Check for updates

Varying the rheological behavior of a micellar solution *via* modified microscopic structures in the presence of graphene oxide†

Takumi Kusano, [ID] * Norihiro Oyama, [ID] Hiroaki Yoshida [ID] and Hiroya Tanaka [ID]

We experimentally and numerically investigate the aggregation structure of cationic wormlike micelles in the presence of graphene oxide (GO), in connection with the change in the rheological properties of their aqueous dispersion. We first confirm that the macroscopic viscoelastic properties under oscillatory shear vary non-monotonically with the addition of GO flakes. We then carried out three distinct experiments—small-angle X-ray scattering (SAXS) measurements, time-domain nuclear magnetic resonance (TD-NMR) measurements, and molecular dynamics (MD) simulations—to elucidate the structural modifications likely responsible for the rheological changes. The results of the SAXS and TD-NMR measurements suggest that surfactant molecules preferentially remain in a worm-like microparticle form when bonded to the GO surface but not completely covering the GO surface. Moreover, using MD simulations, we confirmed that the attractive interaction between negatively charged functional groups on the GO surface and cationic surfactants indeed leads to adsorption. Together with the results of the rheology measurements, the SAXS, TD-NMR, and MD simulation results suggest that GO flakes tend to form three-dimensional aggregates bridged by the wormlike micelles. Our results can be utilized to control the rheological properties of micellar solutions and provide a new paradigm for designing microscopic structures of GO.

1 Introduction

Wormlike micelles, which are formed by surfactants in an aqueous electrolyte solution *via* self-assembled intermolecular aggregation,[1,2] have attracted intensive attention over the past several decades. Various aspects such as thermodynamic, rheological, and structural properties have been investigated not only to achieve fundamental understanding[3–7] but also to explore potential practical applications (*e.g.*, drag reduction agents[3,8] and 3D printing gels[9]). One of the major features of micelles is their abundant structural degrees of freedom,[10,11] which in turn leads to diverse rheological properties.[3,10,12] In particular, Shikata *et al.*[13,14] reported structural modifications of worm-like micelles (*e.g.*, scission and recombination) under steady and oscillatory shear. Such transitions of the micellar structure were shown to be closely related to the rheological property of solutions.[15–18]

Recently, several novel effects related to the electronic and chemical properties of two-dimensional materials, such as graphene and graphene oxide (GO), have been revealed.[19–22]

Toyota Central R&D Labs., Inc., Nagakute, Aichi 480-1192, Japan. E-mail: kusano@mosk.tytlabs.co.jp

These properties are strongly dependent on the physicochemical structures of materials, such as their layering structure, and various techniques for controlling the structures have been explored. For example, several studies[9,23–26] have found that interactions between GO and cationic molecules can modify the layering, structuring, and recovery of GO. Zou *et al.*[23] used a charged polyelectrolyte to assemble three-dimensional structures composed of GO sheets. McCoy *et al.*[25] used cationic surfactants to recover GO and Yue *et al.*[9] applied GO/cationic wormlike micelle dispersions for 3D printing gels. In these systems, the cationic additives are commonly considered to be adsorbed onto GO, which modifies the interaction between the GO surfaces in the aqueous dispersion. Here, the cationic molecules promote the aggregation of GO flakes by destabilizing the dispersed state of them through surface charge neutralization. Importantly, such aggregation of GO flakes then modifies the structure of another major ingredient: micelles of cationic molecules, leading to a change in the macroscopic rheological property. In fact, a recent phenomenological study has shown that GO strongly influences the rheological behavior of cationic wormlike micelle solutions.[27] However, studies on the microscopic structure of cationic worm-like micelles in the presence of these additives remain rare.[25,28]

In the present study, viscoelastic measurements as well as small-angle X-ray scattering (SAXS) measurements, time-domain nuclear magnetic resonance (TD-NMR) spectroscopy

experiments, and molecular dynamics (MD) simulations were performed to investigate the effect of the addition of GO on the rheological and structural behaviors of wormlike micelles in a dispersion of cetyltrimethylammonium bromide (C_{16} TAB), sodium salicylate (NaSal) and GO.

2 Methods

2.1 Experimental

2.1.1 Sample preparation. We prepared the GO/C_{16}TAB/NaSal dispersions (Fig. 1) using the following procedures. C_{16}TAB (Fujifilm Wako Pure Chemical) and NaSal (Fujifilm Wako Pure Chemical) were dissolved in water and a GO dispersion (Merck, 2 mg ml^{-1} dispersion in water) was added dropwise to the prepared C_{16}TAB/NaSal solution. The resultant dispersion was agitated for 24 h using a magnetic stirrer at room temperature and sonicated at a frequency of 20 kHz for 1 h. Experiments were conducted using surfactant, additive salt, and GO dispersions in several different concentration combinations. Specifically, while the molarity of C_{16}TAB, C_D, and that of NaSal, C_S, were kept constant and identical as $C_D = C_S = 100$ mM for all experiments (we provide some results with different value of C_D and C_S in the ESI†), results with various concentrations of GO ($\phi_{GO} = 0$, 0.01, 0.05, and 0.1 wt%) were compared.

2.1.2 Rheology. Rheological properties were measured using a rheometer (MCR302e, Anton Paar) with a cone plate radius of 50 mm and a cone angle of 1°. The frequency dependence of the storage modulus G' and loss modulus G'' were measured at strain $\gamma = 1.0\%$ and frequency ω in the range of between 0.1 and 100 rad s^{-1}. The increment of the frequency at each step was chosen such that the interval was uniform on a base-10 logarithmic scale.

2.1.3 Small angle X-ray scattering. SAXS measurements were performed at the BL8S3 beamline of the Aichi Synchrotron Radiation Center. The scattered X-rays were analyzed with an imaging-plate detector (R-AXIS IV++, Rigaku). The sample-to-detector distance was 1.1 m. The energy and wavelength of the scattered X-rays were 8.2 keV and 1.5 Å, respectively. The scattering vector $q = (4\pi \sin \theta)/\lambda$ was varied in the range 0.02–0.4 Å^{-1}, where 2θ is the scattering angle and λ is the wavelength. Notably, the measured range of the scattering vector enabled

the measurement of lengths from 15 Å to 300 Å, which includes the length scale of C_{16}TAB molecules ($\sim$20 Å) (*i.e.*, the radius of the wormlike micelles). Because the scattering profiles were isotropic, the resultant two-dimensional SAXS images were converted into one-dimensional profiles by circular averaging. The corresponding background intensity of the capillary containing water was subtracted. For absolute intensity calibration, we used glassy carbon NIST Standard Reference Material.

2.1.4 Time-domain nuclear magnetic resonance spectroscopy. NMR spectra were acquired using a MagnoMeter XRS spectrometer (Mageleka). We set the excitation carrier frequency to 12.4 MHz and the excitation-pulse width for 90° to 4.3 μs at 25 °C. We estimated the spin–spin relaxation time, T_2, by analyzing the ^{1}H NMR data using the Carr–Purcell–Meiboom–Gill method. This relaxation time, T_2, becomes shorter when ^{1}H atoms are adsorbed onto the carbon surface.[29] To put it another way, this measurement, usually referred to as the TD-NMR measurement,[29,30] enables a relative estimation of the amount of water molecules adsorbed onto GO surfaces.

2.2 Numerical simulations

We used MD simulations to investigate the interactions between the GO sheets and the surfactant molecules. We considered a system with an aqueous electrolyte solution between two parallel GO membranes. The model GO sheet was composed of pristine graphene sheets with hydroxyl groups, which were placed randomly on the basal plane such that the oxygen content ratio matched that of the commercial GO used in our experiments.[31] The electrolyte solution contained the C_{16}TAB surfactant molecules and the added salt NaBr. The concentrations of C_{16}TAB and NaBr were both 100 mM. Here, we considered a different anion (Br$^-$) for the added salt from the one employed in the experiments for numerical simplicity. The choice of the anion should play only a minor role and not affect the qualitative discussion on the interaction between GO substrates and surfactants here.

All the MD simulations were implemented using the open source code LAMMPS.[32] The water molecules were modeled using the standard SPC/E model.[33] The Lennard-Jones (LJ) parameters of AMBER96 were used for the carbon atoms of graphene, whereas the optimized potentials for liquid simulations all-atom (OPLS-AA) force field[34–36] were used to model the hydroxyl groups, C_{16}TAB molecules, and Na$^+$ and Br$^-$ ions. The partial charges assigned to atoms of C_{16}TAB were taken from the work of Poorgholami-Bejarpasi and Sohrabi,[37] who determined the partial charges using the restrained electrostatic potential (ResP) fitting approach. Throughout the simulations, each graphene sheet was kept rigid, and the hydroxyl group atoms were allowed to move freely. We used the SHAKE algorithm to maintain each water molecule as rigid.[38] Long-range Coulomb interactions were treated by the particle–particle–particle–mesh (PPPM) method. Periodic boundary conditions were assumed in the transverse direction, and the non-periodicity in the longitudinal direction was dealt with by applying the periodic boundary condition with empty spaces outside the sheets. The artifacts from the image charges due to
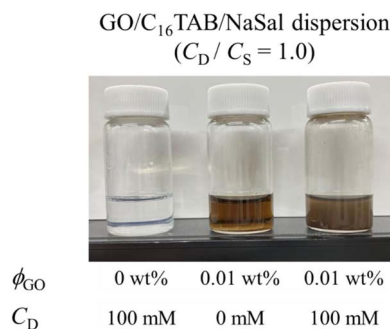

GO/C_{16}TAB/NaSal dispersion
($C_D / C_S = 1.0$)

ϕ_{GO}	0 wt%	0.01 wt%	0.01 wt%
C_D	100 mM	0 mM	100 mM

Fig. 1 GO/C_{16}TAB/NaSal dispersions at $C_D = 100$ mM. The molarity of C_{16}TAB (C_D) was set to be the same as that of NaSal (C_S).

periodic conditions in the transverse direction were removed using the method of Yeh and Berkowitz.[39] The velocity Verlet method was employed for the time integration of the Newton equation for each particle, with a time step of 1 fs. We maintained the temperature at 300 K using the Nose–Hoover thermostat (*i.e.*, canonical ensemble). The production runs were performed for 15 ns after equilibration for at least for 200 ps.

3 Results and discussion

This study aims to use four different measurements to investigate the changes in the rheological and structural properties of micellar solutions as a result of the addition of GO: viscoelastic rheological, SAXS, and TD-NMR experiments and MD simulations. In this section, the results of these measurements are presented.

3.1 Rheology (viscoelasticity)

We first show in Fig. 2 the results of viscoelastic measurements of the $GO/C_{16}TAB/NaSal$ dispersions as a function of the frequency ω. The complex moduli G' and G'' presented here are well described by the single Maxwell model for all values of ϕ_{GO}, which is consistent with the results of wormlike micelle solutions reported by Shikata *et al.*[13] Fitting the results to the single Maxwell model allows us to estimate the stress relaxation time $\tau_R = 2\pi/\omega_{CO}$, where ω_{CO} is the crossover frequency of the storage and loss moduli. The estimated value of τ_R varies non-monotonically with ϕ_{GO}: it first increases with increasing ϕ_{GO} up to 0.05 wt%, then decreases when ϕ_{GO} further changes to 0.1 wt% (Inset of Fig. 2). Notably, this non-monotonic behavior contrasts the monotonic dependence of the viscosity on ϕ_{GO} (see Fig. S1 in ESI†). Since τ_R is proportional to the length of wormlike micelles[40–42] (see eqn (3) appearing later), the results here also suggest that the length of the wormlike micelles

changes non-monotonically with ϕ_{GO} as well. In the following subsection, SAXS measurements were performed to investigate the nanoscale structure of micelles in the presence of graphene oxide.

3.2 SAXS

Fig. 3 shows the scattering intensity $I(q)$ as a function of the magnitude of the scattering vector q, which was obtained from SAXS measurements of the quiescent dispersion with $C_D = 100$ mM. Because the typical scaling behavior $I(q) \propto q^{-1}$ known for rod-like particles[10] is observed for $\phi_{GO} \leq 0.05$ wt% in the low-q region ($q < 0.07$ Å^{-1}), the wormlike micelles are likely to be formed in the $GO/C_{16}TAB/NaSal$ dispersion.

The scattering intensity exhibits another hallmark: we observe a peak at around $q \approx 0.17$ Å^{-1} when GO is present. As reported in several articles[25,43] and demonstrated by our MD simulations later, the GO flakes tend to adsorb the cationic surfactant molecules. This adsorption suppresses the electrostatic repulsion between GO flakes, enabling them to approach each other and allowing van der Waals interaction to become dominant, thereby greatly enhancing the aggregation. In fact, the positions of peaks in the SAXS profiles (Fig. 3), $q \approx 0.17$ Å^{-1}, are in accordance with the first Bragg peak attributed to the interval of the lamellar structure of the GO and $C_{16}TAB$ aggregates.[44] In addition, the peak did not appear in the SAXS profile for the $C_{16}TAB/NaSal$ aqueous solution, and the peak intensity increased in proportion to ϕ_{GO}. These results suggest that the peak is caused by the lamellar structure of GO, which is aggregated by the surfactants. This result is also consistent with the results of a previous study in which the adsorption of
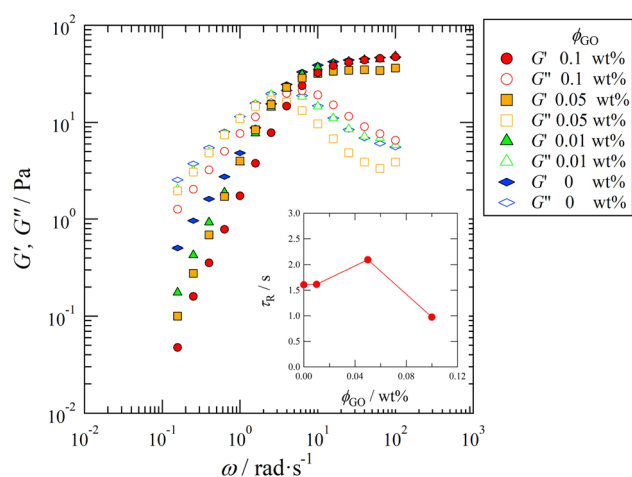

Fig. 2 Log−log plot of the elastic modulus G' and loss modulus G'' as a function of the frequency ω at $C_D = 100$ mM. Symbols distinguish the concentration of the GO, ϕ_{GO}, as indicated in the legend. (Inset) The stress relaxation time $\tau_R = 2\pi/\omega_{CO}$ as a function of ϕ_{GO}. The crossover frequency ω_{CO} is estimated by fitting the results to the single Maxwell model.
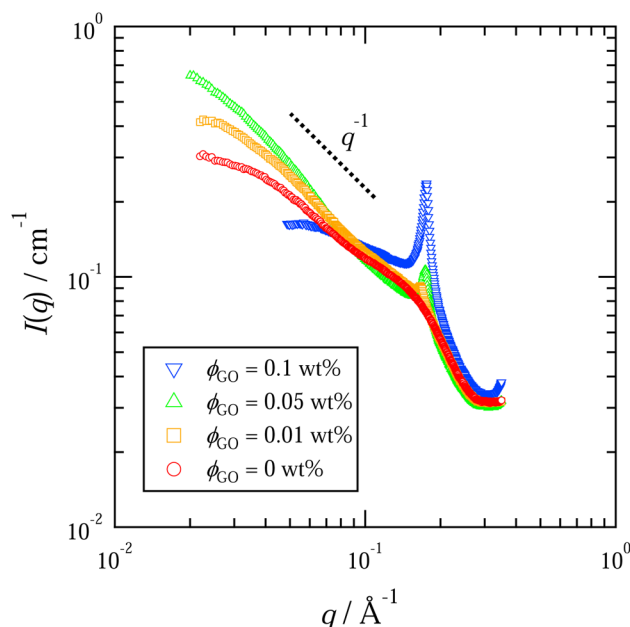

Fig. 3 Scattering intensity $I(q)$ as a function of the magnitude of the scattering vector q. Results for the system with $C_D = 100$ mM are shown. Different symbols represent different concentrations of GO, ϕ_{GO}. The dashed line depicts the inverse proportional scaling relation $I(q) \sim q^{-1}$ that is typical behavior for rod-like particles.

C_{16}TAB onto GO was confirmed to promote the aggregation of GO sheets.[25]

3.3 TD-NMR

We next investigate the spin–spin relaxation time T_2 using TD-NMR measurements. The value of T_2 allows an indirect estimate of the amount of unbound water molecules in the system. In the present study, as explained below, we further utilize T_2 to gain insight into the microscopic structures formed by GO and C_{16}TAB.

Fig. 4 shows the dependence of T_2 on (a) C_D and (b) ϕ_{GO}. In Fig. 4(a), T_2 did not change significantly with respect to C_D. On the other hand, in Fig. 4(b), T_2 decreased monotonically as ϕ_{GO} increased. As shown in Fig. 4(a), the effect of micelle structure or dynamics on T_2 is negligible compared with that of GO concentration. Therefore, the decrease in T_2 with ϕ_{GO} in Fig. 4(b) is attributed to the interaction of water molecules and GO surface. This T_2 decrease with ϕ_{GO} suggests that water molecules tend to be adsorbed on the GO surface. In other words, some adsorption sites on GO are occupied by water molecules even in the presence of C_{16}TAB molecules. That is, the GO surfaces are not completely covered by these surfactants.

3.4 MD simulations

The GO flakes in water exhibit a strong negative surface potential due to the hydroxyl and carboxyl groups at their periphery. Although this resulting negative potential of GO flakes has been considered to attract the cationic surfactant molecules,[25,43] we cannot directly assess the binding tendency experimentally. In the present study, we bypass this technical difficulty using MD simulations and numerically validate the attractive interactions between GO flakes and surfactants. Fig. 5 shows a snapshot of the system considered in our simulations. At the initial setup, C_{16}TAB molecules were located around the center of the slab and were surrounded by water molecules (the number of C_{16}TAB molecules is 6; refer to the caption of Fig. 5 for system details). As the simulation progressed, the C_{16}TAB molecules moved in different random directions because of thermal fluctuations; some of the C_{16}TAB molecules eventually reached the surface of the slab walls. The C_{16}TAB molecules were trapped by the hydroxyl groups on the surface of the GO as a result of electrostatic attraction and the hydrophobic interaction. The trapping of C_{16}TAB molecules is evident in the time evolution of the z-component (direction perpendicular to the GO membranes) of the nitrogen atoms of surfactants shown in Fig. 6. The figure shows that, indeed, once nitrogen atoms approach the GO surface, they cannot escape from it. This observation is strong numerical support for the attraction between GO and surfactant molecules in aqueous solutions.

3.5 Characteristic micellar lengths

The experimental and numerical measurements presented thus far provide us with two different ways to estimate the important microscopic structural information: the characteristic length scale of the wormlike micelles. Importantly, both these two distinct estimations consistently suggest non-monotonic dependence of the characteristic micelle lengths on the GO concentration ϕ_{GO}. In this subsection, we explain the two estimation methods one by one. The first method relies on SAXS
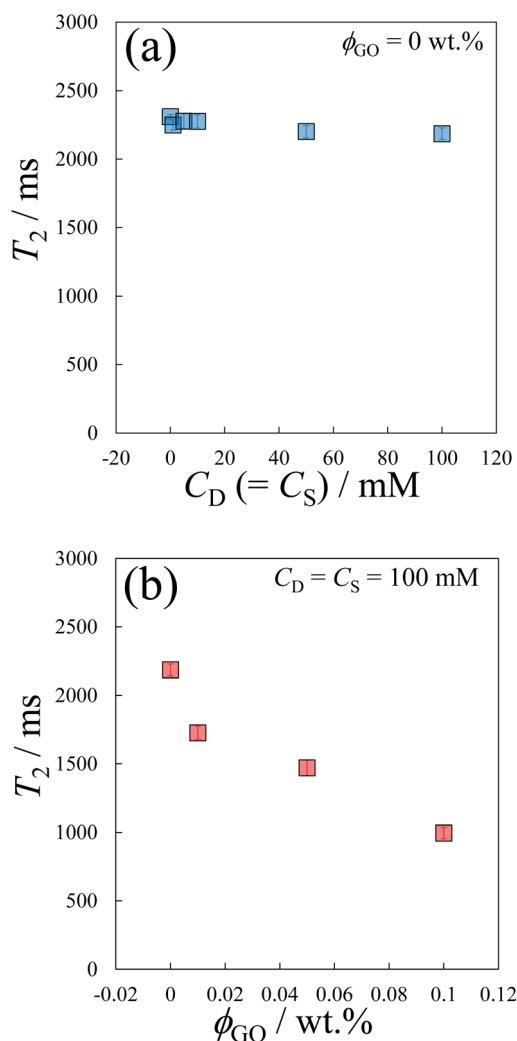

Fig. 4 The relaxation time T_2 as a function of (a) the concentration of surfactant, C_D, and (b) the concentration of GO, ϕ_{GO}. Shades depict the standard errors.
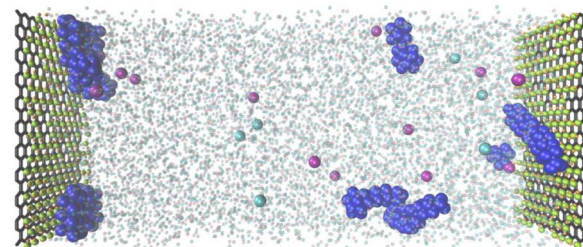

Fig. 5 Snapshot of an MD simulation. Molecules are colored as C_{16}TAB: blue, sodium ion: aqua, bromide ion: purple, hydroxyl groups: pink and yellow. Water molecules are illustrated transparently. The slab size is 24.595 Å × 42.6 Å × 100.64 Å, where the graphene is configured with 10 hexagonal lattices. The numbers of molecules are water: 3094, C_{16}TAB: 6, and NaBr: 6.
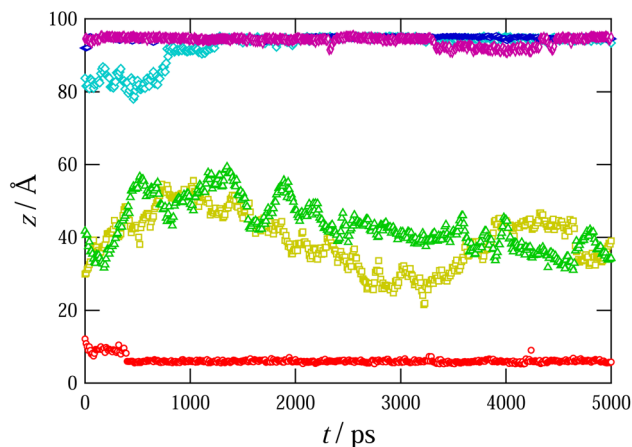
Fig. 6 Time evolution of the positions of the N molecules in the surfactant molecules in the direction perpendicular to the GO membranes (z-direction). Different symbols are used to distinguish different molecules. The GO membranes are located at $z = 0$, 100.64 Å.

profiles. As mentioned above, the peak attributed to the lamellar structure of GO appeared in the SAXS profiles. Therefore, we performed Guinier analysis to separate the scattering profiles of the wormlike micelles from the peak profiles due to the lamellar structure. In Fig. 3, $I(q)$ exhibits a shoulder (Guinier region) attributed to the scattering function of the wormlike micelles in the small-q range of $0.02 \leq q \leq 0.1$ Å^{-1}. A Guinier region provides an estimate of the gyration radius of scattering particles independent of particle shape. According to Guinier's approximation, the scattering function follows eqn (1) in the Guinier region.

$$\ln I(q) = \ln I(0) - \frac{R_g q^2}{3}. \tag{1}$$

Therefore, the gyration radius of particles, R_g, can be calculated from the slope of the Guinier plot.[45,46] Fig. 7(a) shows the Guinier plots based on the SAXS profiles in Fig. 3, with the slope of the fitted lines indicating the gyration radius R_g of the wormlike micelles. For a thin rod, the characteristic micellar length can be written using R_g as follows:[45,46]

$$L_G = \sqrt{12} R_g, \tag{2}$$

where we named the length estimated by this approach L_G. In Fig. 7(b), the obtained value of L_G are plotted as a function of ϕ_{GO}.

The length L_G changes in a non-monotonic fashion, with the maximum value located at $\phi_{GO} = 0.05$ wt%.

The viscoelastic relaxation time τ_R of the wormlike micelles, which was reported in the inset of Fig. 2, can be utilized for the second estimation of the characteristic micellar length which we call L_R as:[40–42]

$$L_R \sim \tau_R \times C_D^{-\frac{3}{4}}. \tag{3}$$

In Fig. 7(b), we compared L_R with L_G. Notice that, since the precise value of L_R can be determined only up to an unknown proportional coefficient, we normalize it as $\tilde{L}_R = L_R \times$
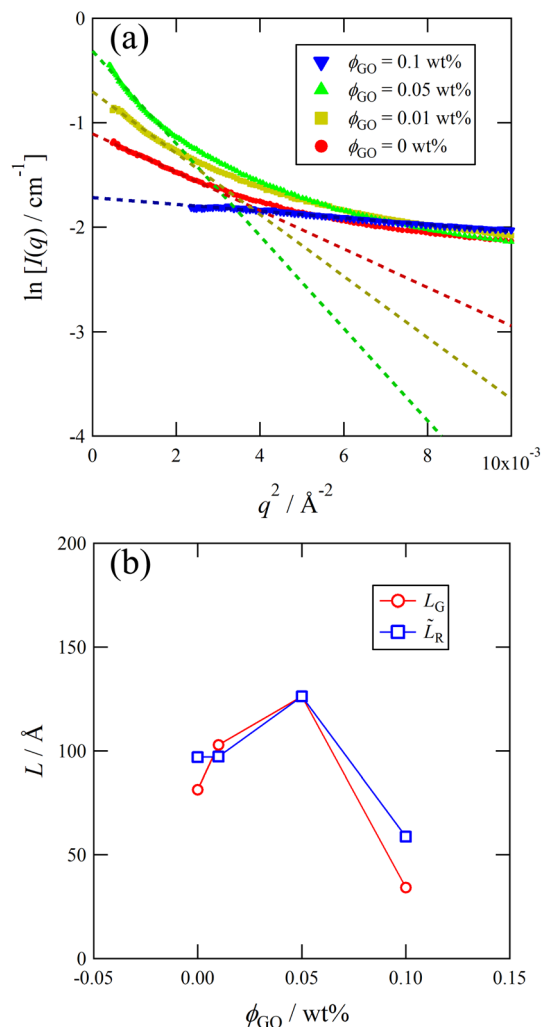

Fig. 7 (a) Guinier plot of SAXS profiles with varying ϕ_{GO}. The dashed line represents the fitted line of the Guinier model. (b) ϕ_{GO} dependence of L_G estimated from Guinier plot and $\tilde{L}_R = L_R \times (L_G^{max}/L_R^{max})$ estimated from viscoelastic measurements.

(L_G^{max}/L_R^{max}), where L_R^{max} and L_G^{max} are the maximum values of two length scales and both of them are the values at $\phi_{GO} = 0.05$ wt%. As can be seen in Fig. 7(b), L_G and L_R consistently indicate the non-monotonic dependence of micelle lengths on the GO concentration ϕ_{GO}.

Now we discuss the cause of such a non-monotonicity of micellar lengths from the viewpoint of the interactions among GO, C_{16}TAB, and NaSal. The results of our MD simulations showed that some surfactant molecules are adsorbed onto GO surfaces at an unassociated state, nor forming micellar structures (we call them "the adsorbed molecules" hereafter). The adsorbed molecules in the unassociated state here means that surfactant molecules that are adsorbed on GO but are not involved in the formation of the wormlike micelles. Since the adsorbed molecules form a lamellar structure with GO without NaSal, the molar ratio of NaSal (salt) to C_{16}TAB (surfactant) in the bulk changes as a function of ϕ_{GO}. The amount of the adsorbed molecules should increase with the concentrations of GO (ϕ_{GO}). And this adsorption results in an increase in the salt-
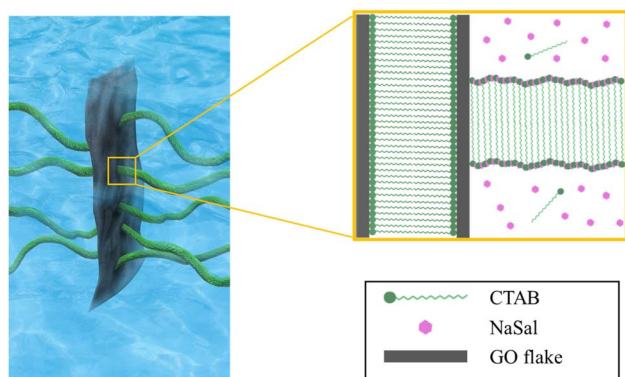
Fig. 8 Schematic of the micellar structure in a GO/C_{16}TAB/NaSal dispersion.

to-surfactant ratio in the bulk. The resulting relative superiority of the salt concentration then leads to an elongation of micelle length, which explains the cause of the experimentally observed increase in micelle length for $\phi_{GO} \leq 0.05$ wt% in Fig. 7(b). If we further increase the GO concentration ϕ_{GO}, another effect becomes dominant: the overall decrease in the surfactant concentration in the dispersion. The surfactant deficiency at high GO concentration would result in shortening effects of micelle length: this is exactly what we observe for the case with $\phi_{GO} = 0.1$ wt%.

3.6 Micellar structure

Finally, we provide a proposed sketch of the microscopic micellar structures in a GO/C_{16}TAB/NaSal dispersion in Fig. 8. Our experiments provide three important implications for the microscopic structures.

First, as discussed in the previous subsection, both the micellar and the unassociated states of surfactant molecules coexist. Second, micelles and GO should self-organize into large aggregates that interfere with the visible light: the formation of large aggregate was evident in Fig. 1 where we visually showed that the GO/C_{16}TAB/NaSal dispersion becomes turbid while pure C_{16}TAB/NaSal solution and GO dispersion were transparent. Considering that the scattering intensity $I(q)$ in Fig. 3 showed a clear peak at around $q = 0.17$ Å^{-1} corresponding to lamellar structure constituting of GO and C_{16}TAB, we propose a stacking structure of surfactants-mediated bilayers of GO connected by the wormlike micelles as shown in Fig. 8. We stress that this structure is consistent with that reported previously.[27,28] Finally, third, we emphasize that GO bilayers are not likely to be fully covered by micelles at least within the parameter space we investigated. This was conjectured based on the TD-NMR measurement results (Fig. 4) that indicated that water molecules occupy a fraction of adsorption sites.

4 Conclusion

We used rheological, SAXS, and TD-NMR measurements, in conjunction with MD simulations, to investigate the aggregation structure of cationic wormlike micelles and GO in aqueous

dispersions. In viscoelastic measurements, the crossover frequency ω_{CO} of G' and G'' first decreases with increasing ϕ_{GO} up to $\phi_{GO} = 0.05$ wt%, then starts increasing, indicating that the length of the wormlike micelles changes in a non-monotonic manner with ϕ_{GO}. TD-NMR measurements were carried out to show that the surfactant molecules cover only part of the GO surface. Moreover, by performing MD simulations, we confirmed that the attractive interaction between negatively charged functional groups of the GO surface and cationic surfactants indeed leads to adsorption, as expected.[25,43] Two micelle length estimated from SAXS profiles and viscoelastic relaxation time are both non-monotonically dependent on ϕ_{GO}. We expect that some of the surfactant molecules are adsorbed onto the surface of GO in an unassociated state. The amount of these adsorbed surfactant molecules simply increases with increasing concentrations of GO (ϕ_{GO}), which results in an increase in the salt-to-surfactant ratio in the dispersion. Because a higher salt concentration corresponds to a longer micelle length, the increase in salt concentration can facilitate micelle elongation. On the other hand, when ϕ_{GO} becomes high, large fraction of surfactant molecules are likely to be adsorbed onto the surface of GO flakes and the lack of surfactant molecules in the solution leads to the shortening of length of the wormlike micelles. Furthermore, together with the results of the rheology, the SAXS, TD-NMR and MD simulation results suggest that GO flakes tend to form a stacking structure of surfactant-mediated bilayers connected by the wormlike micelles. The present results provide a useful paradigm for controlling the rheological properties of micellar solution and designing the microstructure of GO membranes.

Data availability

The data that support the findings of this study are available from the corresponding author on request.

Conflicts of interest

There are no conflicts to declare.

Acknowledgements

Notes and references

1 S. Gravsholt, *J. Colloid Interface Sci.*, 1976, **57**, 575–577.
2 J. Ulmius, H. Wennerstrom, B. Lennart, A. Johansson and G. Lindblom, *J. Phys. Chem.*, 1979, **83**, 2232–2236.

3 *Giant Micelles: Properties and Applications*, ed. R. Zana and E. W. Kaler, CRC Press, Baca Raton, FL, 2007.

4 F. Nettesheim, M. W. Liberatore, T. K. Hodgdon, N. J. Wagner, E. W. Kaler and M. Vethamuthu, *Langmuir*, 2008, **24**, 7718–7726.

5 M. E. Helgeson, T. K. Hodgdon, E. W. Kaler and N. J. Wagner, *J. Colloid Interface Sci.*, 2010, **349**, 1–12.

6 C. A. Dreiss, *Soft Matter*, 2007, **8**, 956–970.

7 C. Dreiss and Y. Feng, *Wormlike Micelles: Advances in Systems, Characterisation and Applications*, Royal Society of Chemistry, Croydon, UK, 2017.

8 J. Yang, *Curr. Opin. Colloid Interface Sci.*, 2002, **7**, 276–281.

9 Q. Yue, Z. Luo, X. Li and L. A. Fielding, *Soft Matter*, 2023, **19**, 6513–6524.

10 M. Takeda, T. Kusano, T. Matsunaga, H. Endo, M. Shibayama and T. Shikata, *Langmuir*, 2011, **27**, 1731–1738.

11 T. Kusano, H. Iwase, T. Yoshimura and M. Shibayama, *Langmuir*, 2012, **28**, 16798–16806.

12 Z. Chu, Y. Feng, X. Su and Y. Han, *Langmuir*, 2010, **26**, 7783–7791.

13 T. Shikata, H. Hirata and T. Kotaka, *Langmuir*, 1987, **3**, 1081–1086.

14 T. Shikata, H. Hirata and T. Kotaka, *Langmuir*, 1989, **5**, 398–405.

15 C. R. Lopez-Barron and N. J. Wagner, *Langmuir*, 2012, **28**, 12722–12730.

16 C. Dai, Y. Zhang, M. Gao, Y. Li, W. Lv, X. Wang, Y. Wu and M. Zhao, *Nanoscale Res. Lett.*, 2017, **12**, 431.

17 K. Morishima, S. Sugawara, T. Yoshimura and M. Shibayama, *Langmuir*, 2017, **33**, 6084–6091.

18 K. Sakai, K. Nomura, R. G. Shrestha, T. Endo, K. Sakamoto, H. Sakai and M. Abe, *Langmuir*, 2012, **28**, 17617–17622.

19 A. H. Castro Neto, F. Guinea, N. M. R. Peres, K. S. Novoselov and A. K. Geim, *Rev. Mod. Phys.*, 2009, **81**, 109–162.

20 D. Chen, H. Feng and J. Li, *Chem. Rev.*, 2012, **112**, 6027–6053.

21 A. Ambrosi, C. K. Chua, A. Bonanni and M. Pumera, *Chem. Rev.*, 2014, **114**, 7150–7188.

22 X. Wang, Z. Li, S. Wang, K. Sano, Z. Sun, Z. Shao, A. Takeishi, S. Matsubara, D. Okumura, N. Sakai, T. Sasaki, T. Aida and Y. Ishida, *Science*, 2023, **380**, 192–198.

23 J. Zou and F. Kim, *Nat. Commun.*, 2014, **5**, 5254.

24 X. Hong, B. Zhang, E. Murphy, J. Zou and F. Kim, *J. Power Sources*, 2017, **343**, 60–66.

25 T. M. McCoy, L. de Campo, A. V. Sokolova, I. Grillo, E. I. Izgorodina and R. F. Tabor, *Phys. Chem. Chem. Phys.*, 2018, **20**, 16801–16816.

26 M. Poorsargol, M. Alimohammadian, B. Sohrabi and M. Dehestani, *Appl. Surf. Sci.*, 2019, **464**, 440–450.

27 A. Bello, J. Ozoani, A. Adebayo and D. Kuriashov, *Petroleum*, 2022, **8**, 522–528.

28 M. E. Helgeson, T. K. Hodgdon, E. W. Kaler and N. J. Wagner, *Langmuir*, 2010, **26**, 8049–8060.

29 C. Takai-Yamashita, J. Ikeda, Y. Wada, Y. Ohya, Y. Yamagata, Y. Takasaki, M. Fuji and M. Senna, *Cellulose*, 2022, **29**, 7049–7062.

30 C. L. Cooper, T. Cosgrove, J. S. van Duijneveldt, M. Murray and S. W. Prescott, *Soft Matter*, 2013, **9**, 7211–7228.

31 N. Fukaya, K. K. H. De Silva, M. Yoshimura and H. Tanaka, *Jpn. J. Appl. Phys.*, 2022, **61**, 095502.

32 A. P. Thompson, H. M. Aktulga, R. Berger, D. S. Bolintineanu, W. M. Brown, P. S. Crozier, P. J. in 't Veld, A. Kohlmeyer, S. G. Moore, T. D. Nguyen, R. Shan, M. J. Stevens, J. Tranchida, C. Trott and S. J. Plimpton, *Comput. Phys. Commun.*, 2022, **271**, 108171.

33 H. J. C. Berendsen, J. R. Grigera and T. P. Straatsma, *J. Phys. Chem.*, 1987, **91**, 6269–6271.

34 W. L. Jorgensen, J. D. Madura and C. J. Swenson, *J. Am. Chem. Soc.*, 1984, **106**, 6638–6646.

35 W. L. Jorgensen, *J. Phys. Chem.*, 2002, **90**, 1276–1284.

36 W. L. Jorgensen, D. S. Maxwell and J. Tirado-Rives, *J. Am. Chem. Soc.*, 1996, **118**, 11225–11236.

37 N. Poorgholami-Bejarpasi and B. Sohrabi, *J. Mol. Model.*, 2013, **19**, 4319–4335.

38 J.-P. Ryckaert, G. Ciccotti and H. J. C. Berendsen, *J. Comput. Phys.*, 1977, **23**, 327–341.

39 I.-C. Yeh and M. L. Berkowitz, *J. Chem. Phys.*, 1999, **111**, 3155–3162.

40 J. F. A. Soltero and J. E. Puig, *Langmuir*, 1996, **12**, 2654–2662.

41 F. Kern, P. Lemarechal, S. J. Candau and M. E. Cates, *Langmuir*, 1992, **8**, 437–440.

42 M. Yamamoto, H. Ando, S. Arima and K. Aramaki, *J. Oleo Sci.*, 2009, **58**, 303–311.

43 T. M. McCoy, H. C. W. Parks and R. F. Tabor, *Carbon*, 2018, **135**, 164–170.

44 W. Meng, E. Gall, F. Ke, Z. Zeng, B. Kopchick, R. Timsina and X. Qiu, *J. Phys. Chem.*, 2015, **119**, 21135–21140.

45 *Methods of X-Ray and Neutron Scattering in Polymer Science*, ed. R. J. Roe, Oxford University Press, New York, 2000.

46 M. C. Lensen, R. J. N. Nolte, A. E. Rowan, W. Pyckhout-Hintzen, M. C. Feiters and J. A. A. W. Elemans, *Dalton Trans.*, 2018, **47**, 14277–14287.